Journal of Physical Science, Vol. 35(2), 47–65, 2024

Microwave Crosslinked Chitosan/Green Fluorescent Carbon Nanoparticles Film: Comprehensive Characterisation and Antimicrobial Performance

Mas Syazlin Masbah,[1] Anwar Iqbal,[1*] Junichi Ida,[2] Rabiatul Basria S. M. N. Mydin,[3] Nur Asshifa Md Noh,[4] Rahadian Zainul,[5,6] and M. Hazwan Hussin[1]

[1]School of Chemical Sciences, Universiti Sains Malaysia, 11800 USM, Pulau Pinang, Malaysia
[2] Faculty of Science and Engineering, Soka University, 1-236 Tangi-machi, Hachioji, Tokyo, 192-8577, Japan
[3] Department of Biomedical Science, Advanced Medical and Dental Institute, Universiti Sains Malaysia, 13200 Kepala Batas, Pulau Pinang, Malaysia.
[4]School of Biological Sciences, Universiti Sains Malaysia, 11800 USM, Pulau Pinang, Malaysia
[5]Department of Chemistry, Faculty of Mathematics and Natural Sciences, Universitas Negeri Padang, Padang, West Sumatra, Indonesia
[6]Centre for Energy and Power Electronics Research, Universitas Negeri Padang, Padang, West Sumatra, Indonesia

[*]Corresponding author: anwariqbal@usm.my

Published online: 31 August 2024

To cite this article: Masbah, M. S. et al. (2024). Microwave crosslinked chitosan/green fluorescent carbon nanoparticles film: Comprehensive characterisation and antimicrobial performance. *J. Phys. Sci.*, 35(2), 47–65. https://doi.org/10.21315/jps2024.35.2.4

To link to this article: https://doi.org/10.21315/jps2024.35.2.4

ABSTRACT: *Conventional crosslinkers used to reduce the swelling of chitosan films are prone to toxicity. Fluorescent carbon nanoparticles, on the other hand, present a safer alternative. This study aims to crosslink microwave-synthesised green fluorescent carbon nanoparticles (GFCNPs) with high quantum yield (44%) and chitosan film via solvent casting (CHT/GFCNPs). The particle size distribution of GFCNPs predominantly ranged from 5 nm to 15 nm. X-ray diffraction (XRD) and high-resolution transmission electron microscopy (HRTEM) analyses indicated the presence of graphite. Attenuated total reflectance-fourier transform infrared (ATR-FTIR) spectroscopy detected various functional groups that enabled crosslinking. The CHT/GFCNPs exhibited significantly lower swelling (500%) compared to chitosan film (2300%). Preliminary findings of antibacterial activity demonstrated the effects of the compounds on bacteria with different*

cell wall structures, namely Gram-positive and Gram-negative bacteria. The CHT/GFCNPs showed potential antibacterial activity against Staphylococcus aureus, a Gram-positive bacteria, compared to Escherichia coli, a Gram-negative bacteria.

Keywords: antimicrobial, chitosan, film, fluorescent carbon nanoparticles, microwave

1. INTRODUCTION

Fluorescence carbon nanoparticles (FCNPs) are a carbon-based nanomaterial with fluorescence properties. The combination of carbon-based material and fluorescence characteristics has attracted interest from academia and industries. In addition to its easy modification, nontoxicity, affordability, less environmentally hazardous and high quantum yield (QY), the FCNPs also have excellent photostability, highly tuneable photoluminescence (PL) properties and good electro-chemiluminescence.[1–3] These features enable the FCNPs to be used in many fields.

Chitosan, derived from the deacetylation of chitin, is a linear semi-synthetic polysaccharide biopolymer extensively employed in the biomedical domain.[4,5] Regardless, chitosan in its original form has low antimicrobial properties and is often combined with other materials to enhance its antimicrobial properties.[6–8] Chitosan incorporated with FCNPs has been used in drug delivery, wound healing, antibacterial treatment, food manufacturing, biochemical analysis, biosensor and bioimaging.[9–15]

Nevertheless, the excessive swelling of chitosan film hampers its application, especially in drug delivery for wound healing treatment. Moisture absorption and retention in the wound area can suppress the healing process by hindering cell migration and tissue regeneration, increasing the risk of infection and causing discomfort to the patient.[16–18] Higher swelling can also cause the film to have poor mechanical properties. Chitosan often modified with crosslinkers to solve this issue. However, currently used crosslinkers are prone to be toxic.[19] Hence, there is an urgent need to find better and safer crosslinkers. Carbonaceous materials such as FCNPs are rich in functional groups and can be an alternative crosslinker to control the swelling behaviour of chitosan films. The FCNPs can also serve as potential antimicrobial agents because of their affinity towards sulfur-rich amino acids, adherence to the microbial cell wall by electrostatic attraction, and disruption of the microbial cytoplasmic membrane and nucleic acids.[20] In addition, the fluorescent features of the FCNPs can be developed to indicate the healing progress.

Therefore, this research is directed towards crosslinking chitosan with green fluorescent carbon nanoparticles (GFCNPs) employing sodium citrate tribasic dihydrate and urea as precursors. Generally, the synthesis of GFCNPs can be done using routes classified into two categories, which are top-down and bottom-up methodologies.[21] The top-down approach prioritises physical methods, such as pulsed laser ablation, arc discharge and ball milling. These techniques involve breaking down larger materials into nanoparticles through mechanical or energetic means. Conversely, the bottom-up approach emphasises chemical methods such as chemical reduction, sonochemical and microwave. These methods involve building up nanoparticles from smaller molecular or atomic components.[22,23] The microwave (MW)-assisted synthesis is highly used in the field of carbon research as carbon materials interact strongly with MW radiation, producing fast heating rates and localised heating along with good control for internal and volumetric heating of materials.[24] The solvent casting method was used to fabricate the chitosan/GFCNPs film (CHT/GFCNPs). The film was characterised using various spectroscopic and microscopic techniques to understand its physicochemical properties. In addition, the potential of the antimicrobial properties of the film were evaluated under dynamic contact conditions by ASTM E2149.

2. EXPERIMENTAL

2.1 Materials and Reagents

Urea [$CO(NH_2)_2$, 99.0%, QRëC, Malaysia], sodium citrate tribasic dihydrate ($C_6H_5Na_30_7 \cdot 2H_2O$, 99.0%, Sigma Aldrich, Belgium), acetic acid (CH_3COOH, 99.8%, QRëC, Malaysia), sodium hydroxide (NaOH, 99.0%, QRëC, Malaysia), chitosan powder (medium molecular weight, Sigma-Aldrich, Iceland) was used without any purification. All the experiments were carried out using ultrapure water (UPW) and distilled water as solvent.

2.2 Synthesis of Green Fluorescent Carbon Nanoparticles

GFCNPs were synthesised using a microwave-assisted synthesis method, adapted with modifications from the approach reported by Nallayagari et al.[25] Urea (5.0 g) and $C_6H_5Na_30_7 \cdot 2H_2O$ (4.0 g) were dissolved in 25 mL of UPW in a 250 mL beaker, placed in a domestic microwave oven, and heated for 20 min at 400 W. A yellow-orange precipitate was formed and allowed to cool and stored in an airtight container covered with aluminium foil.

2.3 Synthesis of Luminescence Chitosan/GFCNPs Film

The solvent casting method was used to synthesise the CHT/GFCNPs as reported method by Hanisah et al. with some modifications.[26] The GFCNPs powder (15 mg) was dissolved in a beaker containing 200 mL 2% w/v aqueous acetic solution. Chitosan (4.0 g) was added, and the mixture was continuously stirred and heated at 50°C for 4 h using a magnetic stirrer with a rate of 200 rpm. The cooled gel solution was centrifuged at 4,000 rpm for 15 min to separate undissolved particles. The film-forming solution was further stirred for 2 h at room temperature to minimise the formation of bubbles. The solution was poured into a teflon mould and dried for 21 h at 50°C. The dried film was neutralised by soaking in sodium hydroxide (NaOH) solution (2% w/v) for 1 min followed by rinsing with distilled water until the pH of the filtrate became neutral. The film was dried at room temperature for 24 h before being placed in the desiccator. The bare chitosan film was prepared without the addition of the GFCNPs.

2.4 Characterisation

The attenuated total reflectance fourier transform infrared spectroscopy (ATR-FTIR, Perkin Elmer, FTIR microscope, Spotlight 200, United States) was used to analyse the functional groups of CHT/GFCNPs between 4,000 cm^{-1}–600 cm^{-1}. Ultraviolet-visible (UV-Vis) absorption spectroscopy was performed on a Perkin Elmer Lambda 35 UV/Vis spectrometer, United States in the range of 200 nm–800 nm. X-ray diffraction (XRD, Bruker D8 Advanced diffractometer, Germany) was used to measure the crystallinity and phase composition of the samples in the range of 5°–95° using CuKα radiation (λ = 0.154 nm). The surface morphology and elemental content of the GFCNPs, and the CHT/GFCNPs were analysed using a scanning electron microscope (SEM, Quanta FEG-650, United Kingdom) and energy-dispersive X-ray spectroscopy (EDX) along with high-resolution transmission electron microscopy (HRTEM, Philips Tecnai G2 F20 microscope, Netherlands). X-ray photoelectron spectroscopy (XPS) analysis was performed on AXIS Ultra DLD, Kratos, United Kingdom. The Al K (1486.6 eV) was used as the X-ray source, and the binding energy was referenced to an adventitious carbon at 284.6 eV. The fluorescence spectra measurement was done using a Perkin Elmer fluorescence spectrophotometer (LS 55, United States).

2.5 Swelling Test

Swelling test was done to study the hydrophilicity of the film and the compatibility between chitosan and GFCNPs. The initial weight of the film was taken, then immersed in a sterile UPW and incubated at 37°C for 1 h. After drying, the

final weight of the film was obtained and used to calculate the swelling capacity. The swelling capacity (S_{eq}) is calculated using the formula given:

$$S_{eq} = \frac{W_s - W_d}{W_d} \times 100\% \quad (1)$$

Where, W_s = weight of the swollen film and W_d = weight of the dry film.

2.6 Photoluminescence Quantum Yield

The QY of the synthesised GFCNPs was determined using quinine sulphate in 0.1 M H_2SO_4 as a reference, which has a known QY of 0.54. The absorption and fluorescence of the quinine sulphate solution were measured across multiple concentration with different absorption values and corresponding fluorescence intensities. The absorption values were plotted against the emission fluorescence peaks to obtain a calibration curve for quinine sulphate.

Next, the GFCNPs solution replaced the quinine sulphate solution, and its absorption value and emission fluorescence peak were measured. The QY of the GFCNPs was calculated using the slope of the plot of fluorescence intensity against absorbance for the GFCNPs, along with the fluorescence peak, absorption value and the known QY of quinine sulphate. This method ensures a reliable and standardised measurement of the QY by comparing it to the known QY of quinine sulphate. The QY was calculated according to the following equation:

$$QY = QY_{reference} \left(\frac{m_{sample}}{m_{reference}} \right) \left(\frac{\eta_{sample^2}}{\eta_{reference^2}} \right) \quad (2)$$

Where, $QY_{reference}$ = 0.54, m = gradient (slope) and η = refractive index.

2.7 Antibacterial Test under Dynamic Contact Condition

The antimicrobial activity was assessed using the ASTM E2149 (ASTM Designation E2149) standard. All glass wares were autoclaved at a temperature of 121℃ and pressure of 15 psi before use. Standard American Type Culture Collection (ATCC) cultures, specifically *S. aureus* ATCC 25923 and *E. coli* ATCC 25922 were utilised in this study. The bacterial cultures were grown aerobically in Luria-Bertani (LB) broth (Merck, Darmstadt, Germany) for 24 h at 37°C. The bacterial stock was stored in a freezer at 4°C. A loopful colonies of the bacterial culture grown on plate were inoculated into LB broth and shaken at 115 rpm at 37±2°C for 18 h–21 h. After that, the test cultures were diluted

into a final concentration of (1.5–3.0) × 10^5 CFU/mL. In order to evaluate the antimicrobial activity, the test samples were added into 250 mL conical flasks containing 50 mL of the bacterial cultures. The conical flasks were shaken at 115 rpm for 15 min before plating for the '0' contact time subgroup. After shaking, 100 µL aliquot of diluted sample mixture was aseptically pipetted onto LB agar to determine the bacterial concentration by spreading it using a sterile cotton bud. The contact time was repeated for 24 h, 48 h and 72 h. The petri dishes with bacterial spread were then incubated at 37±2°C for 24 h. The colonies formed in the petri dishes were converted into colony-forming units per millilitre (CFU/mL). The bacterial inoculum at '0' contact time served as a control and the colonies counted were compared to the colonies formed at control to detect cell growth inhibition. The percentage of bacterial reduction (R%) was calculated using the following equation:

$$R\%\ (CFU/mL) = \left[\frac{(B - A)}{B}\right] \times 100\% \quad (3)$$

Where, R = the antimicrobial rate (%), B = the average number of cell colonies of the sample (CFU/sample) at t_0 contact time and A = the average number of cell colonies of the sample (CFU/sample) at a specified contact time.

3. RESULTS AND DISCUSSION

3.1 Attenuated Total Reflectance-Fourier Transform Infrared Spectroscopy

The Attenuated Total Reflectance-Fourier Transform Infrared (ATR-FTIR) spectra of GFCNPs and CHT/GFCNPs are shown in Figure 1(a). The peaks in the range of 3,600 cm^{-1}–2,500 cm^{-1} are assigned to the hydroxyl (-OH), amine (-NH) and C-H band stretching vibration.[27] The peak at 2,260 cm^{-1} indicates the presence of amino-containing functional groups of nitrile (-C≡N).[28] The peaks located in the spectrum of GFCNPs at 1,665 cm^{-1} and 1,604 cm^{-1} are assigned to C=O, and C=C stretching modes that contributed from, respectively. The sharp peak centred at 1,400 cm^{-1} in the spectrum of GFCNPs is assigned to NH bending or C-N stretching modes.[29] The peaks at 1,305 cm^{-1} and 1,073 cm^{-1} are attributed to the C-N and C-O stretching frequencies, respectively. A peak at 618 cm^{-1} is assigned to the wagging vibrations of O-Na.[30] The presence of these various functional groups enables the GFCNPs to be effectively crosslinked with chitosan, enhancing the material properties of the CHT/GFCNPs composite.

The amino-containing functional group of nitrile (-C≡N) of GFCNPs is invisible in the spectrum of CHT/GFCNPs and the intensity of the peaks in the range of 1,600 cm^{-1}–1,300 cm^{-1} decreased. The changes are due to the bond formation between chitosan and the GFCNPs. The absorption bands at 1,642 cm^{-1}, 1,554 cm^{-1} and 1,406 cm^{-1} are often assigned to amides I, II and III bands, respectively, of chitosan.[31] The IR peak at 2,869 cm^{-1} in the spectrum of CHT/GFCNPs is attributed to the stretching vibration of the saturated C−H bond in chitosan.[30] The IR peaks in the range of 850 cm^{-1}–1,200 cm^{-1} are attributed to the absorption peak of the β-glycosidic bond C−O−C, the in-plane bending vibration peak of the C−H bond in methyl and methylene and the in-plane bending vibration peak of the N−H bond of chitosan.

3.2 X-ray Diffraction Analysis

The XRD diffractograms of GFCNPs and CHT/GFCNPs are shown in Figure 1(b). The XRD peaks $2\theta = 31°$, 42° and 51° are attributed to the hexagonal phase of graphite (JCPDS Card No. 41-1487).[32,33] The broadness of the peaks and weak intensity suggest that GFCNPs has poor crystallinity.[34] Similarly, the diffraction pattern of CHT/GFCNPs suggests a lack of crystallinity.[35] The lack of crystallinity could be due to the formation of intramolecular binding caused by strong intermolecular hydrogen interactions between GFCNPs and chitosan.[36] The interactions changed the chitosan framework to be partially amorphous.[37] As a result, only two peaks can be seen at $2\theta = 20°$ and 22°. The diffraction peaks of the GFCNPs could not be observed, possibly due to the low crystallinity nature of the amorphous GFCNPs and the low amount used compared to chitosan.

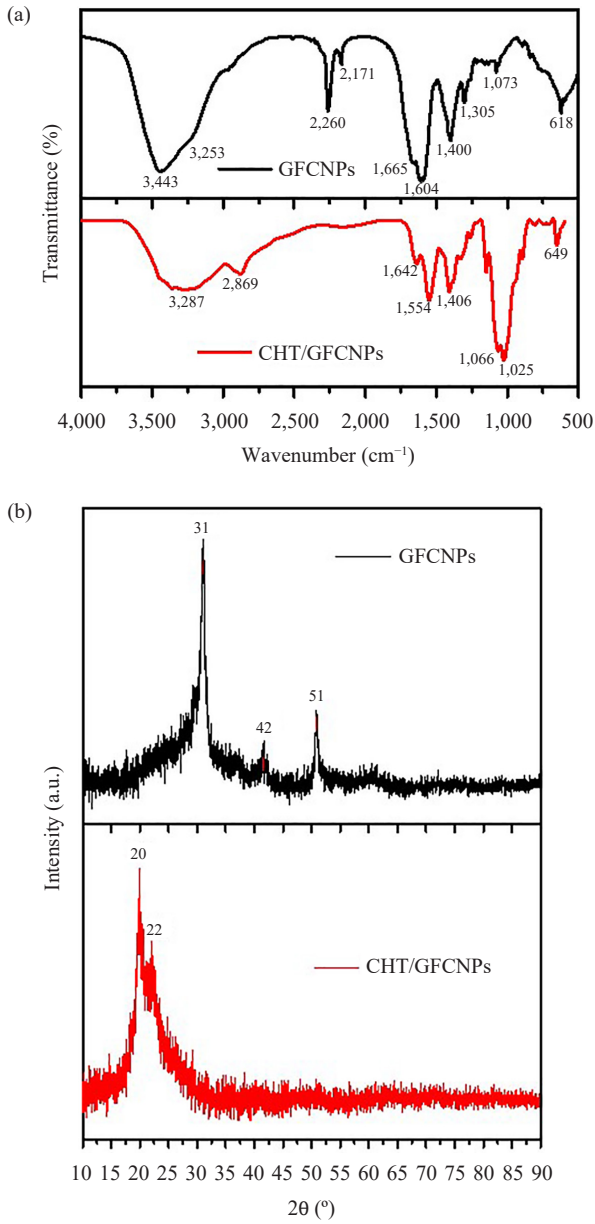

Figure 1: (a) ATR-FTIR spectra and (b) XRD diffractograms of GFCNPs and CHT/GFCNPs.

3.3 Ultraviolet-Visible Absorption Spectroscopic Analysis

The UV-Vis absorption spectrum of GFCNPs is depicted in Figure 2(a). The three notable absorption peaks at 221 nm, 330 nm and 400 nm correspond to specific electronic transitions. The 221 nm absorption band is attributed to the π-π* transition of C=C bonds, and the 330 nm band is linked to the n-π* transition of C=O bonds. The band at 400 nm suggests the presence of a significant conjugated domain.[39] The GFCNPs exhibit a yellowish colour under normal light but fluorescence green under UV light (λ_{ex} = 365 nm).

Only a single absorption peak can be observed in the UV-Vis absorption spectrum of CHT/GFCNPs. The peak is attributed to the π-π* transition of C=C bonds of GFCNPs. The rest of the absorption peak related to CHT/GFCNPs could not be seen, possibly due to bonding with the chitosan framework. The CHT/GFCNPs was observed to exhibit yellow colour under daylight and green fluorescence under 365 nm UV light [as shown in Figure 2(b)].

3.4 Photoluminescence Quantum Yield Analysis

The interpretation of QY with respect to the quinine sulfate reference is shown in Figure 2(b). The QY of GFCNPs was calculated to be 44%. The high QY is due to electron-richness from the nitrogen and oxygen functional groups.[40,41] The higher QY could also be due to microwave irradiation. The $CO(NH_2)_2$ and rapidly reacted together, avoiding sublimation from occurring during the reaction.[42]

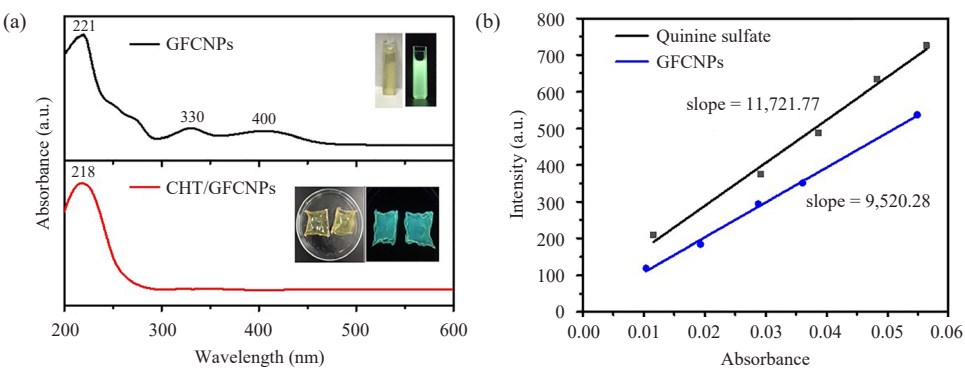

Figure 2: (a) UV-Vis absorbance spectrum and (b) QY of the GFCNPs and reference material. The image of GFCNPs and CHT/GFCNPs under daylight and 365 nm UV light is given in set (a).

3.5 High-resolution Transmission Electron Microscopy and Transmission Electron Microscopy Analysis

The transmission electron microscopy (TEM) image of GFCNPs is shown in Figure 3(a). From the image, the particles are observed to be irregular and quasi-spherically shaped with different sizes without apparent aggregation. The lattice fringes of 0.18 nm determined from the HRTEM image [Figure 3 (b)] is attributed to the graphitic carbon in line with the finding from XRD.[43] The histogram shown in Figure 3(c) indicates that the particle size of GFCNPs was estimated to be predominantly in the range of 5 nm–15 nm.

3.6 Scanning Electron Microscopy-Energy Dispersive X-ray Analysis

The scanning electron microscopy (SEM) analysis indicates that GFCNPs [Figure 3(d)] have an irregular rod-like shape with spore-like ends with pores and voids. However, the SEM image of CHT/GFCNPs [Figure 3(e)] was observed to be smooth without any cracks or voids. The EDX analysis detected C, O, N and Na and the concentration are tabulated in Table 1.

Table 1: Element composition in GFCNPs and CHT/GFCNPs

	Element (%)			
	C	N	Na	O
GFCNPs	36.92	19.07	2.28	41.73
CHT/GFCNPs	59.52	12.84	0.16	27.48

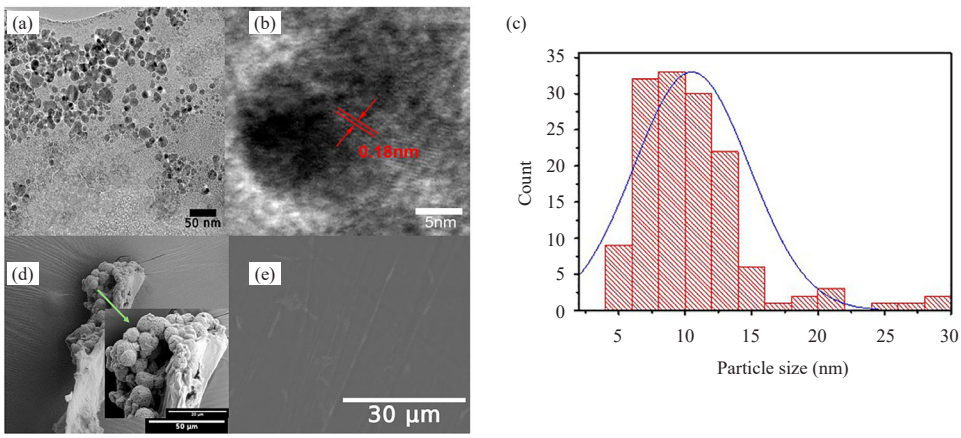

Figure 3: (a) TEM image, (b) HRTEM image and (c) particle size distribution histogram of GFCNPs. The SEM images of (d) GFCNPs and (e) CHT/GFCNPs.

3.7 X-ray Photoelectron Spectroscopy Analysis

The survey spectrum of GFCNPs is shown in Figure 4(a). The detected elements include C, O, N and Na, which is consistent with EDX analysis. The deconvoluted C1s spectrum of GFCNPs [Figure 4(b)] was fitted with three peaks at 284.7 eV, 285.8 eV and 287.9 eV. The peak at 284.7 eV is attributed to the graphitic structure of carbon, indicating that GFCNPs are predominantly composed of carbons.[44] The peaks at 285.8 eV and 287.9 eV are attributed to C-O and C=O groups, respectively.[45] The deconvolution of the O1s peak [Figure 4(c)] resulted in four peaks centred at 535.1 eV, 532.7 eV, 531.6 eV and 530.7 eV. The peak at 535.1 eV was assigned to adsorbed moisture and oxygen.[46] The peak at 531.6 eV is attributed to isolated -OH, C=O and O-C=O groups, while the peak at 532.7 eV is assigned to C-OH and C-O-C functional groups.[47,48] The peak at 530.7 eV can be assigned to Na-O. Deconvolution of the N1s spectrum [Figure 4(d)] indicates the presence of pyridinic nitrogen (397.9 eV), primary/secondary amine nitrogen (399.2 eV) and pyrrolic nitrogen (400.0 eV). The Na1s spectrum [Figure 4(e)] was fitted with a single peak at 1070.1 eV, assigned to bound with oxygen.[49] The XPS findings complement the FTIR results, providing a comprehensive understanding of the chemical composition and functional groups present in the GFCNPs.

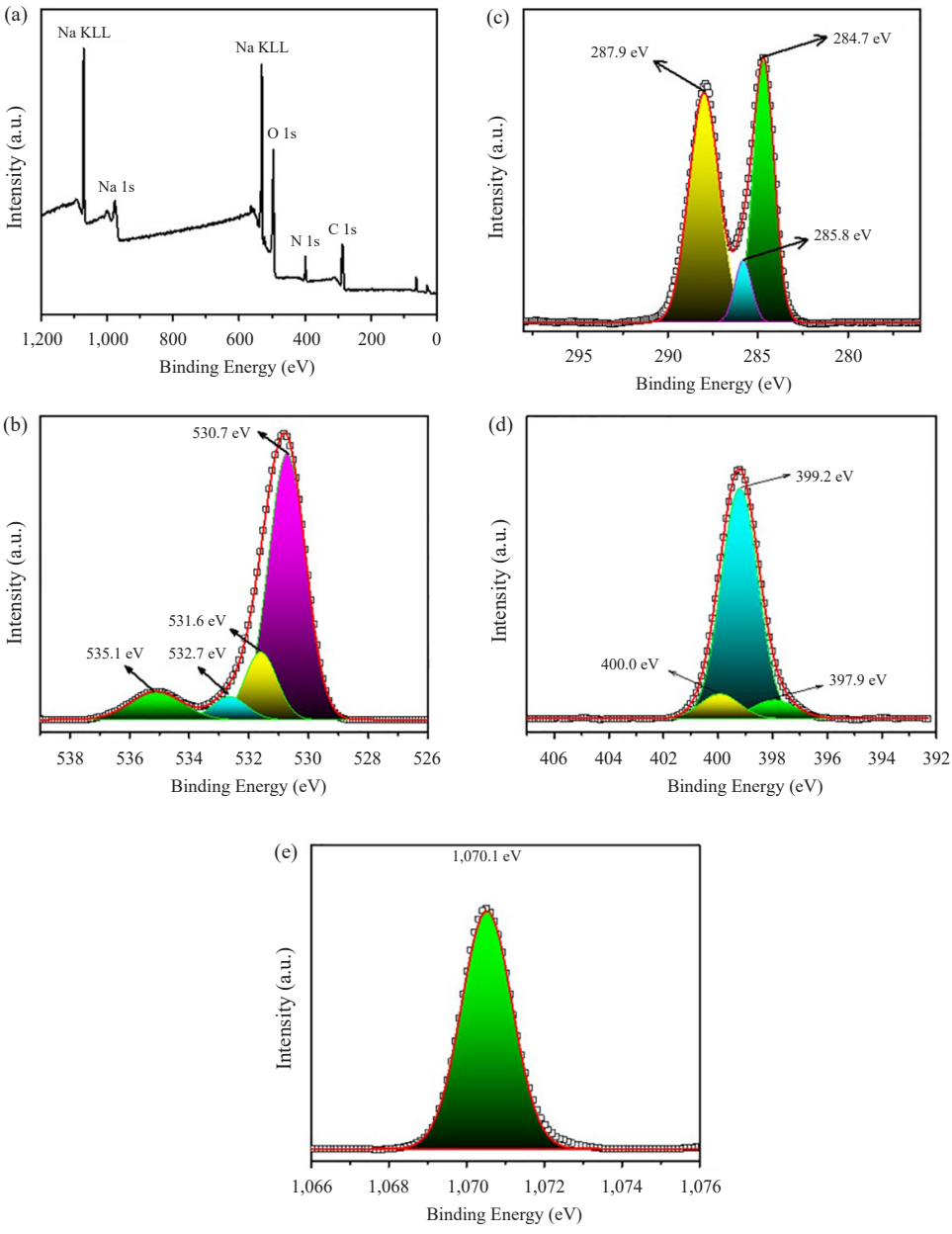

Figure 4: (a) The survey spectrum of GFCNPs, showing the presence of C, O, N and Na. The deconvoluted high-resolution XPS spectra of (b) C1s, (c) O1s, (d) N1s and (e) Na1s of GFCNPs, detail the specific binding energies and corresponding functional groups.

3.8 Swelling Test

The swelling of CHT/GFCNPs was determined to be 500% which is lower compared to bare chitosan film (2300%). The reduction is caused by the utilisation of hydrophilic function groups in the crosslinking process.[50] The outcome indicates successful crosslinking between two components and the film has the potential to be further developed for biomedical applications.

3.9 Antibacterial Test under Dynamic Contact Condition by ASTM E2149

ASTM E2149 is a standard test method designed to evaluate the antimicrobial activity of antimicrobial-treated specimens under dynamic contact conditions. The antibacterial activity of the CHT/GFCNPs was assessed by immersing it in a liquid containing a specific concentration of bacterium inoculum. The immersion increased the surface contact of the polymer sample with water molecules.[51] Bare chitosan film was included for comparison. A log (CFU/mL) against time were plotted for different test bacteria, *S. aureus* and *E. coli*. The plots are shown in Figure 5. The data suggest that there is an antibacterial activity potential against *S. aureus* for CHT/GFCNPs compared to bare chitosan film. However, there is no difference in antibacterial activity for *E. coli* compared to bare chitosan film. This observation might be due to the difference in the cell wall structure of Gram-positive and Gram-negative bacteria. Gram-negative bacteria have an outer membrane composed of lipopolysaccharides, which acts as an additional barrier preventing antimicrobial agent penetration.[52] Generally, this characteristic makes Gram-negative bacteria more resistant to antimicrobial substances than Gram-positive bacteria. This could explain why the compounds tested showed a positive effect of antibacterial activity on *S. aureus* compared to *E. coli.* The figures of bacterial colonies grown on the agar plates are shown in Figure 6.

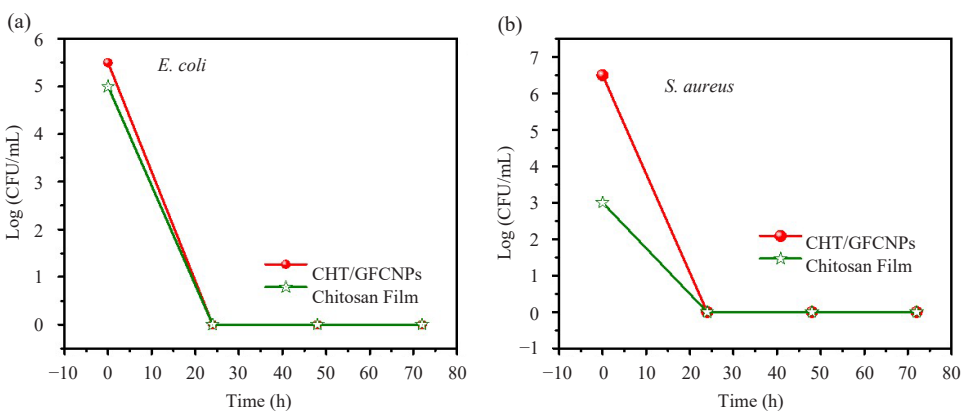

Figure 5: The antimicrobial curve log(CFU/mL) against time for (a) *E. coli* and (b) for *S. aureus* compared with CHT/GFCNPs and chitosan film.

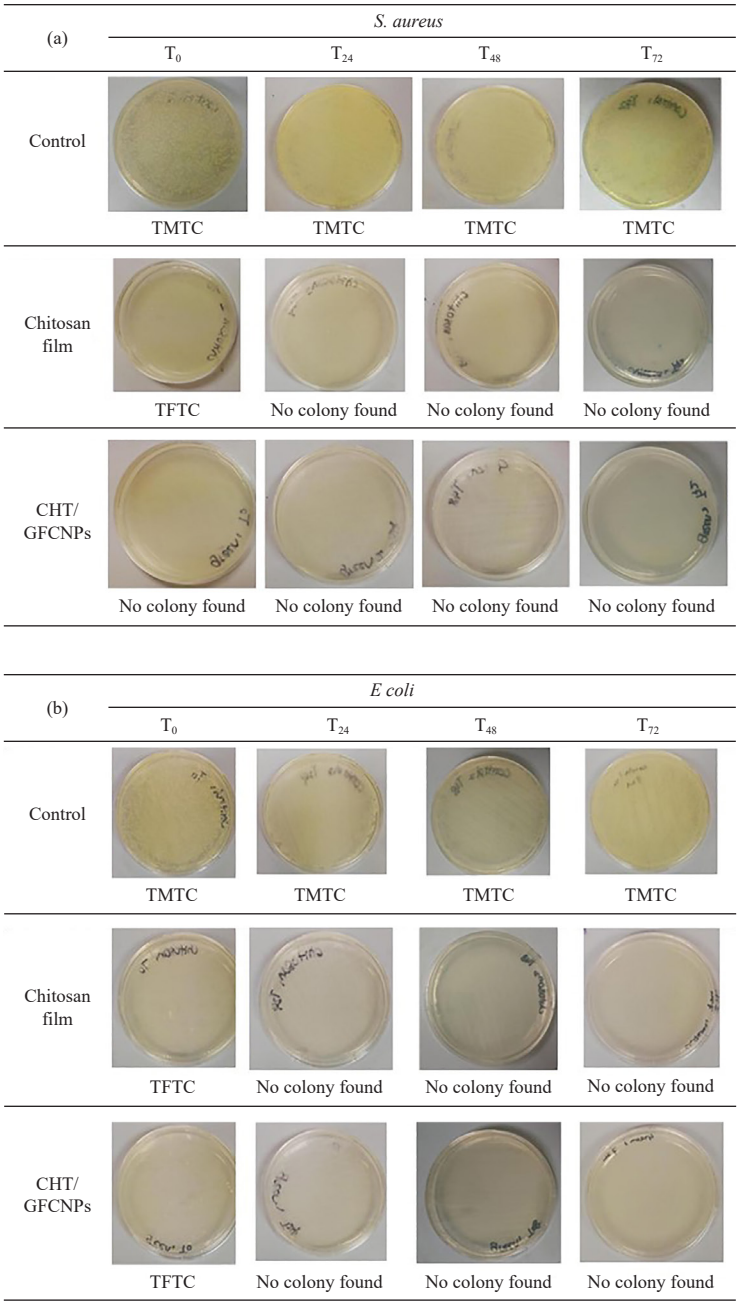

Figure 6: (a) *S. aureus* and (b) *E. coli* bacterial colonies grown on the agar plates.

4. CONCLUSION

GFCNPs and chitosan/GFCNPs were successfully prepared via microwave-assisted and solvent-casting methods. The fluorescence properties of GFCNPs was preserved even after crosslinking with the chitosan film. The fluorescent properties of GFCNPs are attributed to oxygen, nitrogen and sodium. The particle size was predominantly around 5 nm–15 nm. The XRD results reveal an amorphous carbon structure of graphite. The QY of GFCNPs is calculated at 44%. The test results reveal that the swelling of CHT/ GFCNPs in water is reduced compared to pure chitosan, proving that GFCNPs is a good crosslinker. The CHT/GFCNPs showed a potential antimicrobial activity towards *S. aureus*, a Gram-positive bacteria compared to *E. coli*, a Gram-negative bacteria. This is presumably due to the outer membrane of lipopolysaccharides as an additional barrier preventing antimicrobial agent penetration in Gram-negative bacteria. This study indicates CHT/GFCNPs have the potential to be developed in biomedical applications. Regardless, further research is necessary to examine the thermal and mechanical stabilities of the film, as well as the impact of other parameters such as Na concentration, pH, and the presence of ions on the swelling and antimicrobial activities. Additionally, antimicrobial activity can be tested against other different bacterial cultures of Gram-negative and Gram-positive groups.

5. ACKNOWLEDGEMENTS

The authors are thankful to the Ministry of Higher Education of Malaysia for the Fundamental Research Grant Scheme (FRGS/1/2023/STG01/USM/02/2) and Universiti Sains Malaysia for supporting this research.

6. REFERENCES

1. He, C. et al. (2022). The synthetic strategies, photoluminescence mechanisms and promising applications of carbon dots: Current state and future perspective. *Carbon*, 186, 91–127. https://doi.org/10.1016/j.carbon.2021.10.002
2. Yadav, S. & Daniel, S. (2023). Green synthesis of zero-dimensional carbon nanostructures in energy storage applications: A review. *Energy Storage*, 6(1), e500. http://doi.org/10.1002/est2.500
3. Ahmad Najib, M. et al. (2022). Quantum dot-based lateral flow immunoassay as point-of-care testing for infectious diseases: A narrative review of its principle and performance. *Diagnostics*, 12(9), 2158. http://doi.org/10.3390/diagnostics12092158
4. Li, J. et al. (2017). BMP-2 plasmid DNA-loaded chitosan films – A new strategy for bone engineering. *J. Cranio-MaxilloFac. Surg.*, 45(12), 2084–2091. https://doi.org/10.1016/j.jcms.2017.10.005

5. Kandra, R. & Bajpai, S. (2020). Synthesis, mechanical properties of fluorescent carbon dots loaded nanocomposites chitosan film for wound healing and drug delivery. *Arab. J. Chem.*, 13(4), 4882–4894. https://doi.org/10.1016/j.arabjc.2019.12.010
6. Wen, F. et al. (2023). Turmeric carbon quantum dots enhanced chitosan nanocomposite films based on photodynamic inactivation technology for antibacterial food packaging. *Carbohydr. Polym.*, 311, 120784. https://doi.org/10.1016/j.carbpol.2023.120784
7. Villalba-Rodríguez, A. M. et al. (2022). Chitosan-based carbon dots with applied aspects: New frontiers of international interest in a material of marine origin. *Mar. Drugs*, 20(12), 782. https://doi.org/10.3390/md20120782
8. Hüsnügül, Y. A. (2019). Antibacterial activity of chitosan-based systems. In Sougata, J. & Subrata, J. (Eds.). *Functional chitosan: Drug delivery and biomedical applications*. New York: Springer EBooks, 457–489. https://doi.org/10.1007/978-981-15-0263-7_15
9. Ali, A. & Ahmed, S. (2018). A review on chitosan and its nanocomposites in drug delivery. *Int. J. Biol. Macromol.*, 109, 273–286. https://doi.org/10.1016/j.ijbiomac.2017.12.078
10. Augustine, R. et al. (2020). Electrospun chitosan membranes containing bioactive and therapeutic agents for enhanced wound healing. *Int. J. Biol. Macromol.*, 156, 153–170. https://doi.org/10.1016/j.ijbiomac.2020.03.207
11. Hassan, M. A. et al. (2018). Preparation, physicochemical characterisation and antimicrobial activities of novel two phenolic chitosan Schiff base derivatives. *Sci. Rep.*, 8(1), 11416. https://doi.org/10.1038/s41598-018-29650-w
12. Marín, A. C. et al. (2020). Relevance and perspectives of the use of chitosan in winemaking: A review. *Crit. Rev. Food Sci. Nutr.*, 61(20), 3450–3464. https://doi.org/10.1080/10408398.2020.1798871
13. Jaworska, M. M., Antos, D. & Andrzej, G. (2020). Review on the application of chitin and chitosan in chromatography. *React. Funct. Polym.*, 152, 104606. https://doi.org/10.1016/j.reactfunctpolym.2020.104606
14. Sami, B. A. (2017). Nanostructured carbon electrode modified with N-doped graphene quantum dots–chitosan nanocomposite: A sensitive electrochemical dopamine sensor. *R. Soc. Open Sci.*, 4(11), 171199. https://doi.org/10.1098/rsos.171199
15. Tan, L. et al. (2017). Chitosan-based core-shell nanomaterials for pH-triggered release of anticancer drug and near-infrared bioimaging. *Carbohydr. Polym.*, 157, 325–334. https://doi.org/10.1016/j.carbpol.2016.09.092
16. Wang, M. et al. (2021). Nanomaterials applied in wound healing: Mechanisms, limitations and perspectives. *J. Control. Release*, 337, 236–247. https://doi.org/10.1016/j.jconrel.2021.07.017
17. Rajendran, N. K. et al. (2018). A review on nanoparticle based treatment for wound healing. *J. Drug Deliv. Sci. Technol.*, 44, 421–430. https://doi.org/10.1016/j.jddst.2018.01.009
18. Stoica, A. E., Chircov, C. & Grumezescu, A. M. (2020). Nanomaterials for wound dressings: An up-to-date overview. *Molecules*, 25(11), 2699. https://doi.org/10.3390/molecules25112699

19. Kandra, R. & Bajpai, S. (2020). Synthesis, mechanical properties of fluorescent carbon dots loaded nanocomposites chitosan film for wound healing and drug delivery. *Arab. J. Chem.*, 13(4), 4882–4894. https://doi.org/10.1016/j.arabjc.2019.12.010
20. Shilpa, B. M. et al. (2023). Eco-friendly synthesized nanoparticles as antimicrobial agents: An updated review. *Front. Cell. Infect. Microbiol.*, 13, 1224778. https://doi.org/10.3389/fcimb.2023.1224778
21. Chakraborty, N. et al. (2022). Green synthesis of copper/copper oxide nanoparticles and their applications: A review. *Green Chem. Lett. Rev.*, 15(1), 187–215. https://doi.org/10.1080/17518253.2022.2025916
22. Chae, A. et al. (2017). Microwave-assisted synthesis of fluorescent carbon quantum dots from an A2/B3 monomer set. *RSC Adv.*, 7(21), 12663–12669. https://doi.org/10.1039/c6ra28176a
23. Janus, Ł. et al. (2019). Chitosan-based carbon quantum dots for biomedical applications: Synthesis and characterisation. *Nanomaterials*, 9(2), 274. https://doi.org/10.3390/nano9020274
24. Singh, R. et al. (2019). Progress in microwave-assisted synthesis of quantum dots (graphene/carbon/semiconducting) for bioapplications: A review. *Mater. Today Chem.*, 12, 282–314. https://doi.org/10.1016/j.mtchem.2019.03.001
25. Nallayagari, A. R. et al. (2021). Tuneable properties of carbon quantum dots by different synthetic methods. *J. Nanostructure Chem.*, 12(4), 565–580. https://doi.org/10.1007/s40097-021-00431-8
26. Ibrahim, N. H. et al. (2022). Photocatalytic remediation of harmful *Alexandrium minutum* bloom using hybrid chitosan-modified TiO_2 films in seawater: A lab-based study. *Catalysts*, 12(7), 707. https://doi.org/10.3390/catal12070707
27. Pete, A. M. et al. (2023). Biogenic synthesis of fluorescent carbon dots (CDs) and their application in bioimaging of agricultural crops. *Nanomaterials*, 13(1), 209. https://doi.org/10.3390/nano13010209
28. Bipin, R. & Mandal, U. (2023). A review on characterisation of carbon quantum dots. *Vietnam J. Chem.*, 61(6), 693–718. https://doi.org/10.1002/vjch.202300022
29. Rezaei, A., Elham, K. & Seyed M. Z. (2023). Investigating of the influence of zinc oxide nanoparticles morphology on the properties of electrospun polyvinyl alcohol/chitosan (PVA/CS) nanofibers. *J. Drug Deliv. Sci. Technol.*, 86, 104712. https://doi.org/10.1016/j.jddst.2023.104712
30. Azhary, S. Y. et al. (2019). Synthesis and characterisation of chitosan: SiO_2 nanocomposite by ultrasonic spray drying. *IOP Conf. Ser.: Mater. Sci. Eng.*, 550(1), 012037. https://doi.org/10.1088/1757-899X/550/1/012037
31. Zhang, Y. et al. (2016). Effect of reaction temperature on structure and fluorescence properties of nitrogen-doped carbon dots. *Appl. Surf. Sci.*, 387, 1236–1246. https://doi.org/10.1016/j.apsusc.2016.07.048
32. Jayapriya, J. et al. (2012). Preparation and characterisation of biocompatible carbon electrodes. *Compos. B Eng.*, 43(3), 1329–1335. https://doi.org/10.1016/j.compositesb.2011.10.019
33. Taspika, M. et al. (2020). Influence of TiO_2/Ag particles on the properties of chitosan film. *Adv. Nat. Sci. Nanosci. Nanotechnol.*, 11(1), 015017. https://doi.org/10.1088/2043-6254/ab790e

34. Abdouss, H. et al. (2023). Green synthesis of chitosan/polyacrylic acid/graphitic carbon nitride nanocarrier as a potential pH-sensitive system for curcumin delivery to MCF-7 breast cancer cells. *Int. J. Biol. Macromol.*, 242, 125134. https://doi.org/10.1016/j.ijbiomac.2023.125134
35. Kaczmarek, M. B. et al. (2019). Enzymatic modifications of chitin, chitosan, and chitooligosaccharides. *Front. Bioeng. Biotechnol.*, 7, 243. https://doi.org/10.3389/fbioe.2019.00243
36. Cai, L. et al. (2019). Characterisation of gelatin/chitosan ploymer films integrated with docosahexaenoic acids fabricated by different methods. *Sci. Rep.*, 9(1), 8375. https://doi.org/10.1038/s41598-019-44807-x
37. Shehap, A. M. et al. (2021). Preparation and characterisations of high doping chitosan/MMT nanocomposites films for removing iron from ground water. *J. Environ. Chem. Eng.*, 9(1), 104700. https://doi.org/10.1016/j.jece.2020.104700
38. Vercelli, B. et al. (2021). Nitrogen-doped carbon quantum dots obtained hydrothermally from citric acid and urea: The role of the specific nitrogen centers in their electrochemical and optical responses. *Electrochim. Acta*, 387, 138557. https://doi.org/10.1016/j.electacta.2021.138557
39. Mohammad, J. M. (2019). Carbon quantum dots and their biomedical and therapeutic applications: A review. *RSC Adv.*, 9(12), 6460–6481. https://doi.org/10.1039/c8ra08088g
40. Ding, H. et al. (2020). Surface states of carbon dots and their influences on luminescence. *J. Appl. Phys.*, 127(23). https://doi.org/10.1063/1.5143819
41. Manioudakis, J. et al. (2019). Effects of nitrogen-doping on the photophysical properties of carbon dots. *J. Mater. Chem. C*, 7(4), 853–862. https://doi.org/10.1039/C8TC04821E
42. Omar, N. A. S. et al. (2022). A review on carbon dots: Synthesis, characterisation and its application in optical sensor for environmental monitoring. *Nanomaterials*, 12(14), 2365. https://doi.org/10.3390/nano12142365
43. Li, Z. et al. (2021). Green synthesis of carbon quantum dots from corn stalk shell by hydrothermal approach in near-critical water and applications in detecting and bioimaging. *Microchem. J.*, 166, 106250. https://doi.org/10.1016/j.microc.2021.106250
44. Ma, X. et al. (2019). Synthesis of luminescent carbon quantum dots by microplasma process. *Chem. Eng. Process. - Process Intensifi.*, 140, 29–35. https://doi.org/10.1016/j.cep.2019.04.017
45. Lai, C.-W. et al. (2012). Facile synthesis of highly emissive carbon dots from pyrolysis of glycerol; gram scale production of carbon dots/mSiO_2 for cell imaging and drug release. *J. Mater. Chem.*, 22(29), 14403. https://doi.org/10.1039/c2jm32206d
46. Smith, M. et al. (2016). Improving the deconvolution and interpretation of XPS spectra from chars by ab initio calculations. *Carbon*, 110, 155–171. https://doi.org/10.1016/j.carbon.2016.09.012
47. Dager, A. et al. (2019). Synthesis and characterisation of mono-disperse carbon quantum dots from fennel seeds: Photoluminescence analysis using Machine Learning. *Sci. Rep.*, 9(1),14004. https://doi.org/10.1038/s41598-019-50397-5

48. Vedamalai, M. et al. (2014). Carbon nanodots prepared from O-phenylenediamine for sensing of ions in cells. *Nanoscale*, 6(21), 13119–13125. https://doi.org/10.1039/c4nr03213f
49. Rami, V. et al. (2015). High performance Na_xCoO_2 as a cathode material for rechargeable sodium batteries. *J. Mater. Chem. A*, 3(35), 18059–18063. https://doi.org/10.1039/c5ta03173g
50. Hong, F. et al. (2024). Chitosan-based hydrogels: From preparation to applications, a review. *Food Chem*. *X*, 21, 101095. https://doi.org/10.1016/j.fochx.2023.101095
51. Abu, D. I. et al. (2019). The dominant role of surface functionalisation in carbon dots' photo-activated antibacterial activity. *Int. J. Nanomed.*, 14, 2655–2665. https://doi.org/10.2147/ijn.s200493
52. Malmir, S. et al. (2020). Antibacterial properties of a bacterial cellulose CQD-nanocomposite. *Carbohydr. Polym.*, 234, 115835. https://doi.org/10.1016/j.carbpol.2020.115835